Vortex lines nearly parallel to the surface of a single-crystal superconductor disk in a perpendicular field

Katsuhiro Kawashima
School of Bionics, Tokyo University of Technology, 1404-1 Katakura, Hachioji, Tokyo 192-0982, Japan

Oliver B. Wright
Department of Applied Physics, Faculty of Engineering, Hokkaido University, Sapporo 060-8628, Japan
(Received 24 January 2003; revised manuscript received 23 June 2003; published 18 November 2003)

Using a contact-free ultrasonic method we obtain strong experimental evidence that vortex lines penetrating into a type-II single-crystal superconductor disk in a perpendicular dc magnetic field lie during the virgin magnetization stage nearly parallel to the surface over a substantial area of the sample. This phenomenon is very different from the predictions of various existing theoretical models in which the vortex lines are inclined at significant angles to the disk plane. We demonstrate that this phenomenon continues until the applied field is increased to a magnitude that correlates with the lower critical field H_{c1}.

DOI: 10.1103/PhysRevB.68.184511 PACS number(s): 74.25.Qt, 74.25.Op

INTRODUCTION

Type-II superconductor samples for magnetization measurements are often thin platelets of thickness much smaller than the transverse dimensions, for example thin disks or strips, which are put into a perpendicular magnetic field to obtain a larger magnetic signal. Therefore the study of the properties of vortex lines in thin platelets is important from a scientific as well as a practical point of view.

In this perpendicular geometry the original Bean model does not apply because of the large and nonuniform demagnetization effect associated with such thin samples. There have been significant recent developments on the theory of vortex lines in thin platelets in a perpendicular field.[1–5] In these theories the vortex lines are inclined at significant angles to the disk plane in a perpendicular field.

In this paper we report unusual vortex line behavior involving penetration into a single-crystal Nb disk in a perpendicular dc-magnetic field, in which the vortex lines lie during the virgin magnetization stage nearly parallel to the surface over a substantial area of the sample.

Detection is achieved by a totally contact-free ultrasonic method, sensitive to both the in-plane and out-of-plane orientations of the vortex lines, in which the ultrasonic wave is generated and detected through mutual conversion between the ultrasonic wave and the magnetic field associated with the vortex lines. A recently reported contact-free ultrasonic method[6,7] for superconductors uses a contact-free coil to generate ultrasonic waves and a contact quartz transducer to detect them and vice versa. How a totally contact-free ultrasonic method used in this paper can detect the vortex line directions inside a superconductor is explained next.

CONTACT-FREE ULTRASONICS FOR SUPERCONDUCTORS

Figure 1 shows how ultrasonic waves can be generated through the interaction of the applied ac magnetic field with the penetrated vortex lines. In Fig. 1, the surface and near-surface regions of an infinite superconductor plate are shown, and the surface is parallel to the xy plane. The superconductor plate is assumed to be isotropic for every material characteristic (apart from the elastic properties). The thickness of the plate, d, is very much larger than the real part $\mathrm{Re}(\lambda_{ac})$ of the complex ac penetration depth λ_{ac}. The vortex lines uniformly distributed with induction $B=n\phi_0$ are parallel to the xz plane and make an angle α to the surface normal (z direction). Here, ϕ_0 is the flux quantum and n is the vortex line density measured at the plane perpendicular to the vortex direction. The ac magnetic field b_0 (x direction, angular frequency ω) parallel to the sample surface is applied by the ac current I_C in an infinite plane coil that consists of straight wires directed along the y direction and extending in the xy plane. If the vortex lines are pinned elastically, the ac magnetic field b penetrates exponentially according to the complex ac penetration depth λ_{ac}.[8,9] λ_{ac} approximately has the same value for any value of the angle α (Refs. 8 and 10):

$$b=b_0\exp(-\lambda_{ac}z). \tag{1}$$

The ac magnetic field b generates the screening current J_S (y direction) which exerts Lorentz forces on the vortex lines. The Lorentz force F per unit length of a vortex line is proportional to the flux quantum ϕ_0 and to J_S which is proportional to b with a proportionality constant K_1:

$$F=J_S\phi_0=K_1 b\phi_0=K_1\phi_0 b_0\exp(-\lambda_{ac}z). \tag{2}$$

The Lorentz force is perpendicular to the vortex lines, and it is transferred to the material lattice through the mechanical

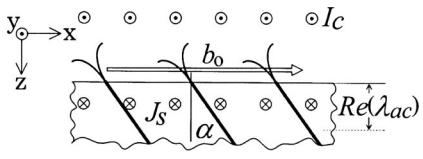

FIG. 1. Contact-free generation and detection of ultrasonic waves for a type-II superconductor through mutual conversion between ultrasonic waves and the magnetic field associated with vortex lines.

coupling between the vortex lattice and pinning sites. Therefore the force F_V per unit volume given to the material lattice is

$$F_V = nF = K_1 n b \phi_0 = K_1 n \phi_0 b_0 \exp(-\lambda_{ac} z). \quad (3)$$

$\mathrm{Re}(\lambda_{ac})$ of single-crystalline Nb is estimated to be a few micrometers[11] at 4.2 K and at frequencies of MHz order. $\mathrm{Re}(\lambda_{ac})$ is negligible compared to the ultrasonic wavelength (shear wavelength, about 0.2 mm, and longitudinal wavelength, about 0.5 mm, at 10 MHz for Nb) and the forces acting on the material lattice from the pinning sites can be integrated with respect to depth giving rise to an effective surface force F_S as an ultrasonic wave source:

$$F_S = \int_0^\infty F_V dz = \int_0^\infty K_1 n \phi_0 b_0 \exp(-\lambda_{ac} z) dz$$
$$= K_1 n \phi_0 b_0 / \lambda_{ac}. \quad (4)$$

The surface forces normal and tangential to the surface, F_{SN} and F_{ST}, are given by

$$F_{SN} = F_S \sin\alpha = K_1 n \phi_0 b_0 \sin\alpha / \lambda_{ac}, \quad (5)$$

$$F_{ST} = F_S \cos\alpha = K_1 n \phi_0 b_0 \cos\alpha / \lambda_{ac}. \quad (6)$$

Constraining the surface forces to be equal to the stresses associated with the ultrasonic waves generated at the surface yields the longitudinal and shear ultrasonic-wave amplitudes

$$u_l(z) = i(F_{SN}/\rho V_l \omega)\exp(-ik_l z)$$
$$= i(K_1 n \phi_0 b_0 \sin\alpha / \rho V_l \omega \lambda_{ac})\exp(-ik_l z), \quad (7)$$

$$u_s(z) = i(F_{ST}/\rho V_s \omega)\exp(-ik_s z)$$
$$= i(K_1 n \phi_0 b_0 \cos\alpha / \rho V_s \omega \lambda_{ac})\exp(-ik_s z). \quad (8)$$

Here, $u_l(z)$ and $u_s(z)$ are the displacement fields of the ultrasonic waves. V_l and V_s are the longitudinal and shear ultrasonic wave speeds, and k_l and k_s are the longitudinal and shear ultrasonic wave numbers, respectively. ρ is the density. Equations (7) and (8) are essentially the same as Eq. (2) given in Ref. 6.

Through the inverse physical process, the mutual interaction between the vortex lattice and ultrasonic waves that takes place within the ac penetration depth on the other side of the infinite superconductor plate produces a radiation of an ac magnetic field into the vacuum which is detected by an identical infinite plane coil placed there. The radiated ac magnetic field is proportional to the ultrasonic displacement and to the static magnetic field associated with the vortex lines.[6] Therefore the detected voltage amplitude E_l (which is proportional to the radiated ac magnetic field) for the longitudinal waves is proportional to $u_l(d)$ and the tangential component of the magnetic field $B\sin\alpha = n\phi_0 \sin\alpha$,

$$E_l = K_2 u_l(d) n \phi_0 \sin\alpha$$
$$= K_3 i \exp(-ik_l d) b_0 (n\phi_0 \sin\alpha)^2 / \lambda_{ac} \rho V_l, \quad (9)$$

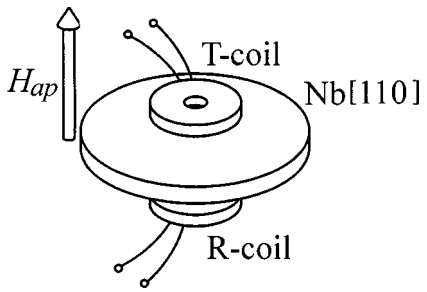

FIG. 2. Experimental setup for contact-free generation and detection of ultrasonic waves for a single-crystal Nb disk in a perpendicular field. Nb disk (purity 99.9%, diameter 12 mm, thickness 0.51 mm, and with surface normal [110]). *T*-coil and *R*-coil (diameter 6.5 mm, with nine turns). Gap between each coil and the surface (0.2 mm).

and that for the shear ultrasonic wave E_s is proportional to $u_s(d)$ and the normal component of the magnetic field $B\cos\alpha$:

$$E_s = K_2 u_s(d) B \cos\alpha$$
$$= K_3 i \exp(-ik_s d) b_0 (n\phi_0 \cos\alpha)^2 / \lambda_{ac} \rho V_s. \quad (10)$$

Here K_2 is a constant and $K_3 = K_1 K_2 / \omega$.

The absolute value of the ratio of E_l to E_s is calculated as

$$|E_l / E_s| = (V_s / V_l)\tan^2\alpha. \quad (11)$$

Thus, we see that the ratio of E_l to E_s can determine the orientation α of the vortex lines within the ac penetration depth range in the case of infinite plane coils, an infinite superconductor plate, and uniformly distributed vortex lines. Equation (11) cannot generally be used in the case of disk coils and a disk sample as used in the experiment, but it can be used in an important special case explained next.

In Fig. 2, a transmitting disk coil (*T* coil) is placed in a coaxial orientation near a superconductor disk. A similar receiving coil (*R* coil) is placed in a symmetrical position on the other side of the superconductor. An external dc magnetic field H_{ap} is applied perpendicular to the superconductor surface. We assume that the single-crystal Nb used in the experiment is nearly isotropic as regards vortex line penetration so that the vortex lines are spatially distributed symmetrically with respect to the center axis.

In such a case if only longitudinal waves and no shear waves are detected ($E_s = 0$), it is self-evident that all the vortex lines beneath the coil are aligned at the same angle 90°. In another words all the vortex lines lie parallel to the surface at least within the ac penetration depth. Likewise, if only shear waves and no longitudinal waves are detected ($E_l = 0$), it can be concluded that all the vortex lines beneath the coil have only components normal to the surface. In other words the angle to the surface normal α is 0°. This method is called, for brevity, EMAT-SC (electromagnetic-acoustic transduction in superconductors) in this paper.

DETECTION OF THE VORTEX LINE DIRECTIONS: EXPERIMENT

A single-crystal Nb disk (purity 99.9%, diameter 12 mm, thickness 0.51 mm, and with the surface normal [110]) was cooled in a zero field (ZFC) down to 4.2 K, and then a uniform dc magnetic field was applied perpendicular to the disk plane. The reason for choosing a sample with the surface normal [110] is to ensure that all three ultrasonic polarizations (longitudinal, fast shear, and slow shear waves) traveling along the [110] direction have different wave speeds. For other symmetry directions ([100] and [111]) the two shear waves degenerate into one shear wave. We can collect more information by choosing the [110] direction. The uniform dc magnetic field was increased from 0 kG up to 6 kG and then decreased to 0 kG in steps of 0.2 kG to 1 kG, at the same temperature. A transmitting disk coil (T coil, diameter 6.5 mm, with nine turns) was placed near one surface with a gap of 0.2 mm. A similar receiving coil (R coil) was placed in a symmetrical position on the other side of the sample with the same gap. (See Fig. 2.) ac currents applied to the T coil generate a circular shielding current near the surface of the sample in the mixed state. The shielding current exerts a Lorentz force on the vortex lines, and it is transferred to the material lattice through the mechanical coupling between the vortex lattice and pinning sites. We assume that the single-crystal Nb used in the experiment is nearly isotropic as regards to vortex line penetration, so that the vortex lines are spatially distributed in a symmetric way with respect to the center axis. Therefore the surface force obtained by integrating the Lorentz force with respect to depth has tangential and normal components F_{ST} and F_{SN} as depicted in Fig. 3. Here F_{SN} is the source of longitudinal ultrasonic waves and F_{ST}, which has only a radial component, is the source of shear ultrasonic waves. F_{ST} is divided into two mutually orthogonal in-plane components F_{STX} and F_{STY}, and generates two shear waves through the acoustic birefringence effect. The two shear waves are polarized along the material symmetry directions [001] and $[1\bar{1}0]$, respectively. The T-coil current frequency was scanned in a 5-MHz range between 7 and 12 MHz. During the scanning, the thickness resonance condition $kd = m\pi$ is satisfied for particular values of k, where k is the ultrasonic wave number, d is thickness, and m is a positive integer, thereby generating a standing wave and greatly improving the generation efficiency. The generated ultrasonic wave moves the vortices at the opposite surface of the sample and thereby generates an ac magnetic field in free space that is detected by the R coil. At a given frequency a burst sinusoidal excitation of duration 20 μs (long enough to establish a standing wave) is used and detection is achieved by monitoring the induced voltage in the R coil, gating the coil output for a 20-μs duration starting 1 μs after the burst ends. In this respect the excitation and detection processes are in fact separated in time, and the detected voltage amplitude is proportional to that of the acoustic contribution during excitation. In another words, immediately after the sinusoidal excitation burst in the T coil ends the ac magnetic field ceases to exist but acoustic standing waves remain in the sample for a while (a few tens of microseconds) until they die out by acoustic attenuation. These remaining acoustic waves move the vortex lines and are detected by gating the R coil. Thus, the detected ac signal voltage is solely due to the acoustic wave and possible environmental noise, and nothing else. It is now clear that this is not simply a popular eddy current measurement and differs significantly from that. Ultrasonic data are obtained as detected voltage amplitude versus frequency. A similar detailed description of the measurement method has been given in the context of a normally conducting metal sample.[12]

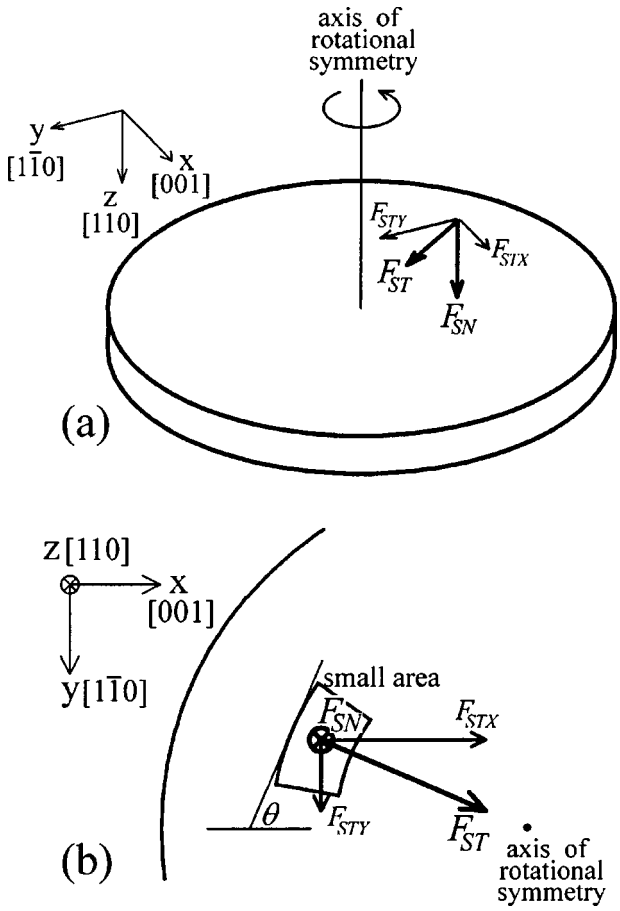

FIG. 3. (a) The surface forces acting on the sample surface obtained by integrating the Lorentz force with respect to depth. F_{SN} is normal to the surface and is the source of longitudinal ultrasonic waves. F_{ST} is tangential to the surface and has only a radial component. F_{ST} is divided into two mutially orthogonal in-plane components F_{STX} and F_{STY}, which generate two shear waves through the acoustic birefringence effect. The two shear waves are polarized along the material symmetry directions, [001] and $[1\bar{1}0]$, respectively. (b) The surface forces just beneath a small area of the T coil. The direction of a small wire element in the small area makes an angle θ with the [001] direction.

Figures 4(a), 4(b), and 4(c) were obtained at 4.2 K under applied magnetic fields H_{ap} of 0.8 kG, 1.6 kG, and 5 kG, respectively, during the increasing dc magnetic field stage. Since the detected voltage amplitude is proportional to ultrasonic-wave amplitude [Eqs. (9) and (10)], the vertical axes of Figs. 4(a), 4(b), and 4(c) are set as the ultrasonic-wave amplitude. These vertical axes are normalized by a

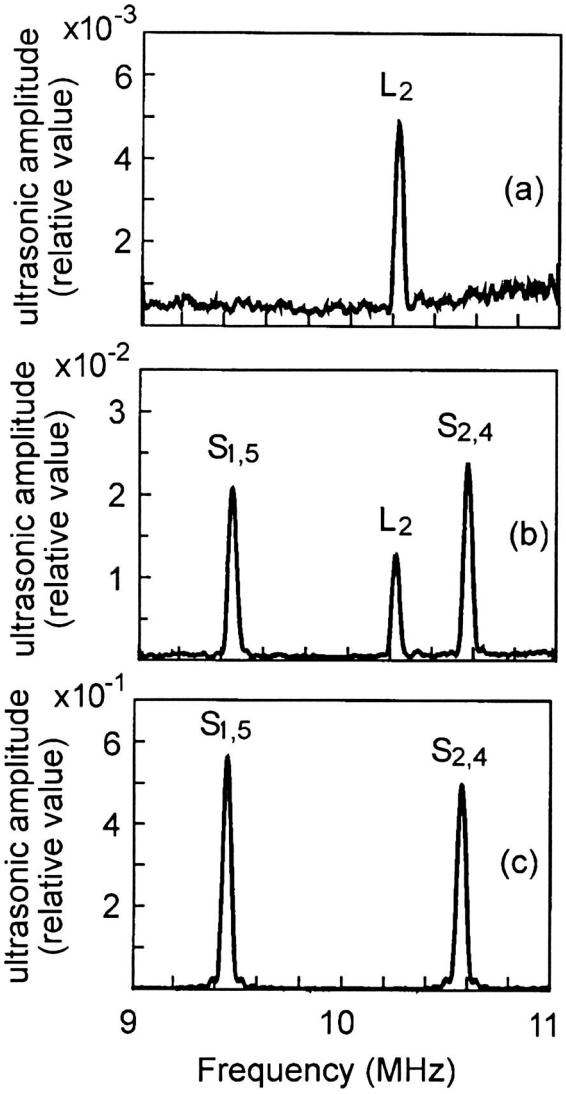

FIG. 4. Resonant peaks for contact-free ultrasonics obtained on single-crystal Nb in the superconducting state (4.2 K). The sample was cooled in zero field (ZFC) down to 4.2 K, and then a uniform dc magnetic field was applied perpendicular to the disk plane. L_2 is the second-order longitudinal resonance. $S_{1,5}$ and $S_{2,4}$ are the fifth- and fourth-order shear resonances. (a) Only longitudinal waves were obtained under 0.8 kG, (b) both longitudinal waves and shear waves were obtained under 1.6 kG, and (c) only shear waves were obtained under 5 kG. Vertical axes of (a),(b),(c) are normalized by a certain common value. The same value is also used to normalize the vertical axes of other figures (Figs. 5, 7, 8, 9, 10, 12, and 13): therefore all these vertical axes may be directly compared.

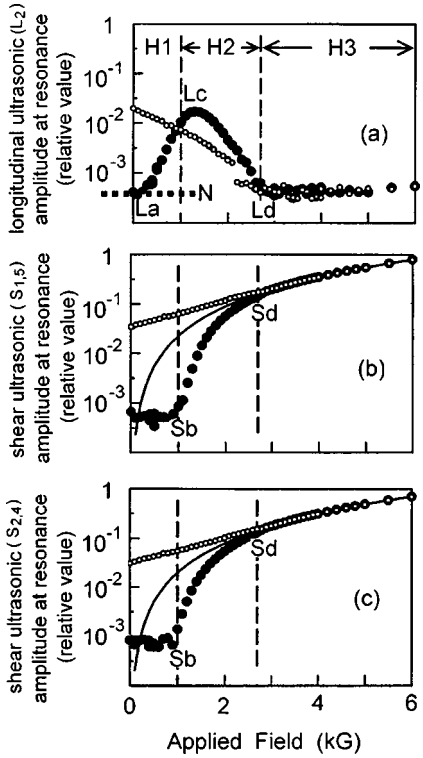

FIG. 5. Resonant peak amplitude for contact-free ultrasonics vs the applied dc magnetic field H_{ap} at 4.2 K. The sample was cooled in zero field (ZFC) down to 4.2 K, and then a uniform dc magnetic field was applied perpendicular to the disk plane. (a) The second-order longitudinal resonant peak L_2, (b) the fifth-order shear resonant peak $S_{1,5}$, and (c) the fourth-order shear resonant peak $S_{2,4}$. Solid circles and open circles correspond to increasing and decreasing fields, respectively. The thick horizontal dotted line N in (a) is the noise level. The thin solid curve in (b) and (c) is a square law curve $A \propto H_{ap}^2$.

certain common value. The same value is also used to normalize the vertical axes of the other figures (Figs. 5, 7, 8, 9, 10, 12, and 13), and therefore all these vertical axes may be directly compared. The following remarkable findings are revealed: one can see only a longitudinal wave in Fig. 4(a), both longitudinal and shear waves in Fig. 4(b), and only shear waves in Fig. 4(c). Here $S_{1,5}$ and $S_{2,4}$ are the fifth- and fourth-order shear resonance and L_2 is the second-order longitudinal resonance. The resonance orders were determined by the number of resonance peaks obtained at lower frequencies. The waves corresponding to $S_{1,5}$ and $S_{2,4}$ are polarized along [001] and $[1\bar{1}0]$, respectively. These waves can be identified by their wave velocities $V=2fd/m$, where f is the resonance frequency. The frequencies obtained at 4.2 K for L_2, $S_{1,5}$, and $S_{2,4}$ in Fig. 4(b) are, respectively, 10.23, 9.46, and 10.57 MHz, with corresponding velocities 5220, 1930, and 2700 m/s. These velocites are nearly equal to but a little larger than the calculated velocities 5030, 1820, and 2570 m/s obtained using the known single-crystal elastic constants of Nb at room temperature,[13] as expected from the difference in temperature. Similar velocity values were obtained in Figs. 4(a) and 4(c). Changes in amplitude at resonance due to the dc-magnetic field change are shown in Fig. 5: Figures 5(a), 5(b), and 5(c), respectively, show the longitudinal-wave amplitudes at resonance corresponding to L_2 and the shear-wave amplitudes at resonance corresponding to $S_{1,5}$ and $S_{2,4}$ versus the applied dc magnetic field H_{ap} at 4.2 K. Solid circles and open circles correspond to increasing and decreasing fields, respectively. The increase in field and decrease in field took place each over a time interval longer than 60 min. This was sufficiently slow for the results to be independent of this time. The thick horizontal dotted line N represents the noise level. There are three distinct H_{ap} ranges

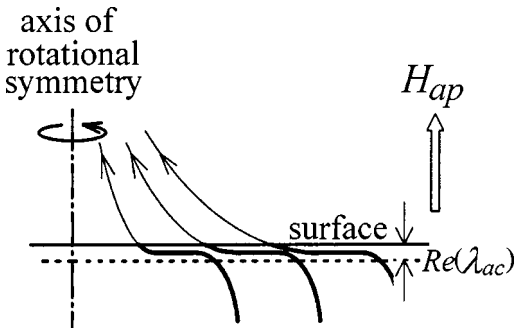

FIG. 6. Sketch of vortex lines parallel to the surface of a disk superconductor in a perpendicular field. The vortex lines lie parallel to the surface within the ac penetration depth range during the virgin magnetization stage. The circular central area of the sample facing the *T* or *R* coil is shown. The vortex line dimensions and the actual distribution drawn are arbitrary.

in the case of increasing field. In the first range below 1 kG ($H1$) only longitudinal waves are obtained [Fig. 5(a)], in the second range between 1 kG and 2.7 kG ($H2$) both longitudinal and shear waves are obtained [Figs. 5(a), 5(b), and 5(c)], and in the third range above 2.7 kG ($H3$) only shear waves are obtained [Figs. 5(b) and 5(c)]. In Fig. 5(a) we see that when H_{ap} is increased to 0.4 kG (point L_a) a longitudinal wave L_2 appears above the noise level N. Here L_2 in Fig. 4(a) was obtained ($H_{ap}=0.8$ kG) in this first range $H1$. It grows larger as H_{ap} is increased. At about 1.3 kG (point L_c), it reaches a maximum value, and then becomes smaller as H_{ap} is further increased. It vanishes at 2.7 kG (point L_d) at the end of $H2$ and does not appear again on further increasing the field. L_2 in Fig. 4(b) was obtained ($H_{ap}=1.6$ kG) in this second range $H2$. On decreasing the field L_2 appears again at 2.7 kG, grows larger as the field is decreased down to 0 kG, and retains an appreciable value at 0 kG. In Fig. 5(b) the shear wave $S_{1,5}$ is absent at low values of H_{ap}, and only appears when H_{ap} is increased to 1 kG (point S_b), defining the beginning of $H2$.

$S_{1,5}$ in Fig. 4(b) was obtained ($H_{ap}=1.6$ kG) in this second range $H2$. It grows larger as H_{ap} is increased and joins a square-law curve [$A \propto H_{ap}^2$, the thin solid curve in Fig. 5(b)] at 2.7 kG (point S_d) at the end of $H2$ and the beginning of $H3$, and continues to grow larger until the maximum applied field (6 kG) is reached. $S_{1,5}$ in Fig. 4(c) was obtained ($H_{ap}=5$ kG) in this third range $H3$. As H_{ap} is decreased from 6 kG to 2.7 kG (point S_d), it decreases following a similar path to that for increasing field. As H_{ap} is further decreased down to 0 kG it continuously decreases but along a different path from the square-law curve and from the path for increasing field, showing significant hysteresis. It retains an appreciable value at 0 kG. In Fig. 5(c) the shear wave $S_{2,4}$ follows a similar path to $S_{1,5}$. Here $S_{2,4}$ in Fig. 4(b) and in Fig. 4(c) was obtained in the second range $H2$ and the third range $H3$, respectively.

VORTEX LINES NEARLY PARALLEL TO THE DISK SURFACE IN A PERPENDICULAR FIELD

We propose the following interpretation: vortex lines begin penetration at a very low field H_{ap} because of the large demagnetizing factor, but these vortex lines lie nearly parallel to the surface at least within the range of the ac magnetic field penetration depth over a substantial area of the sample facing the coil until H_{ap} is increased to 1 kG at 4.2 K. This can be inferred because only longitudinal waves and no shear waves are detected in $H1$ as shown in Figs. 4 and 5.

A sketch how such vortex lines should be arranged is shown in Fig. 6 in which we assume that single-crystal Nb is nearly isotropic as regards vortex line penetration, so that the vortex lines are spatially distributed with axial symmetry. Detecting no shear waves does not necessarily mean that no shear waves are generated in the sample because there may be a small shear-wave signal hidden under the noise level N. This possibility is discussed later.

As H_{ap} is increased above 1 kG new vortex lines keep penetrating, and the vortex lines inside begin to move to a perpendicular configuration. This can be inferred because both longitudinal and shear waves are detected in $H2$. The ratio of these two polarizations changes as the field is further increased. Just before H_{ap} reaches the end of $H2$ [points L_d in Fig. 5(a) and S_d in Fig. 5(b)], all the vortex lines stand perpendicular to the surface, and then the sample shifts to the normal state. This is deduced because only shear waves are detected at the upper end of $H2$. In the third range ($H3$) only shear waves are detected because the EMAT-SC mechanism is taken over by another mechanism appropriate for the normal state [which we refer to simply as EMAT (Refs. 12 and 14)], as explained later. The end of the second range corresponds to the higher critical field H_{c2}. All the wave polarizations are detected after decreasing the field to 0 kG because vortex lines are trapped with finite angles in the sample by pinnning effects. We also attribute all other hysteretic effects to these pinning effects.

To investigate the generality of these phenomena at different temperatures, we also carried out similar measurements at 5 K and 6 K (ZFC and then a uniform dc magnetic field was applied perpendicular to the disk plane). Figures 7(a), 7(b), and 7(c) were obtained at 5 K under applied magnetic fields H_{ap} of 0.7 kG, 1.4 kG, and 5 kG, respectively, during the increasing dc-magnetic field stage. Figures 8(a), 8(b), and 8(c) were obtained at 6 K under applied magnetic fields H_{ap} of 0.5 kG, 0.8 kG, and 5 kG, respectively, during the increasing dc magnetic field stage. One can see only a longitidinal wave in Fig. 7(a) and in Fig. 8(a), both longitudinal and shear waves in Fig. 7 (b) and in Fig. 8(b), and only shear waves in Fig. 7(c) and in Fig. 8(c). Similar velocity values to those (5220, 1930, and 2700 m/s) obtained at 4 K [Figs. 4(a), 4(b), and 4(c)] are obtained at 5 K [Figs. 7(a), 7(b), and 7(c)] and at 6 K [Figs. 8(a), 8(b), and 8(c)].

Figures 9(a), 9(b), and 9(c) respectively show the longitudinal-wave amplitudes at resonance corresponding to L_2 and the shear-wave amplitudes at resonance for $S_{1,5}$ and $S_{2,4}$ versus the applied dc magnetic field H_{ap} at 5 K. Solid circles and open circles correspond to increasing and decreasing fields, respectively. Figures 10(a), 10(b), and 10(c) show the data obtained at 6 K. One can also see the same three ranges in Figs. 9 and 10 as seen in Fig. 5, the first range ($H1$) in which only longitudinal waves are obtained [Figs. 9(a) and 10(a)], the second range ($H2$) in which both longi-

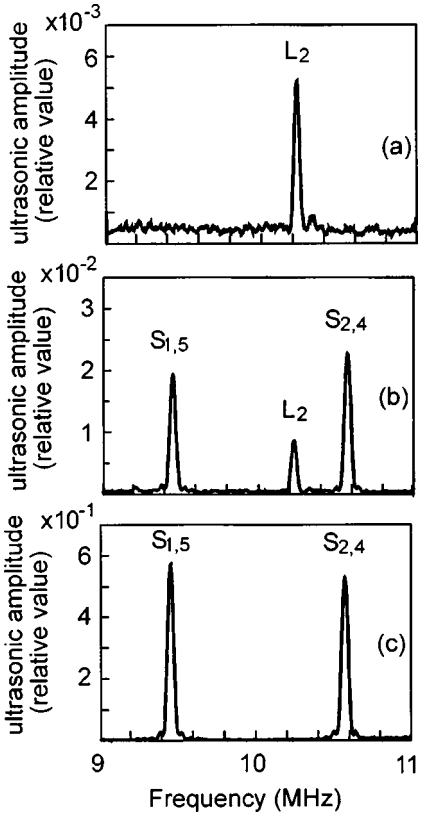

FIG. 7. Resonant peaks for contact-free ultrasonics obtained on single-crystal Nb in the superconducting state (5 K). The sample was cooled in zero field (ZFC) down to 5 K, and then a uniform dc magnetic field was applied perpendicular to the disk plane. L_2 is the second-order longitudinal resonance. $S_{1,5}$ and $S_{2,4}$ are the fifth- and fourth-order shear resonance. (a) Only longitudinal waves were obtained under 0.7 kG, (b) both longitudinal waves and shear waves were obtained under 1.4 kG, and (c) only shear waves were obtained under 5 kG.

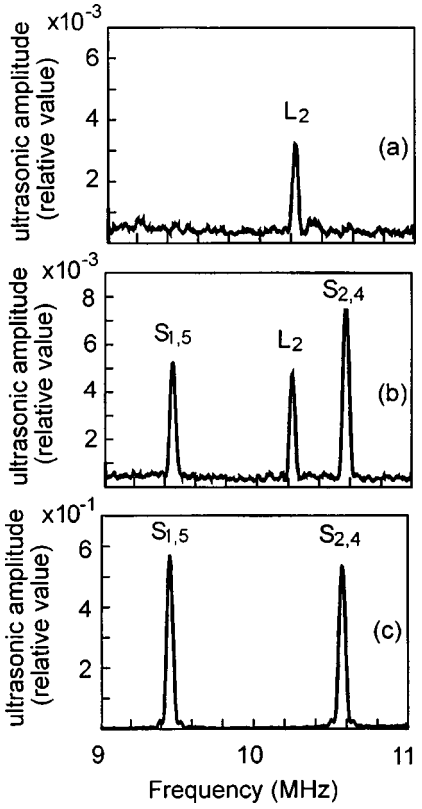

FIG. 8. Resonant peaks for contact-free ultrasonics obtained on single-crystal Nb in the superconducting state (6 K). The sample was cooled in zero field (ZFC) down to 6 K, and then a uniform dc magnetic field was applied perpendicular to the disk plane. L_2 is the second-order longitudinal resonance. $S_{1,5}$ and $S_{2,4}$ are the fifth- and fourth-order shear resonances. (a) Only longitudinal waves were obtained under 0.5 kG, (b) both longitudinal waves and shear waves were obtained under 0.8 kG, and (c) only shear waves were obtained under 5 kG.

tudinal and shear waves are obtained [Figs. 9(a), 9(b), 9(c) and Figs. 10(a), 10(b), 10(c)], and the third range ($H3$) in which only shear waves are obtained [Figs. 9(b), 9(c) and 10(b), 10(c)]. But the extent of the three ranges is found to be different: $H1$, $H2$, and $H3$ at 5 K are below 0.8 kG, between 0.8 and 2.1 kG, and above 2.1 kG, respectively. The corresponding ranges at 6 K are below 0.6 kG, between 0.6 and 1.2 kG, and above 1.2 kG, respectively. The ends of the first range $H1$ at 4.2 K, 5 K, and 6 K correspond to 1 kG, 0.8 kG, and 0.6 kG, respectively. The end field of the first range $H1$ versus temperature is shown in Fig. 11. The thin solid curve is calculated from the standard expression for the lower critical field $H_{c1}(T)=H_{c1}(0)\{1-(T/T_c)^2\}$, where $H_{c1}(0)$ and T_c are taken as 1.2 kG and 9.25 K, respectively. $H_{c1}(0)$ for Nb has been found in the range of 1.1–1.8 kG (Ref. 15). Figures 6 and 11 suggest that the penetrating vortex lines lie parallel to the surface at least within the ac magnetic field penetration depth during the virgin magnetization stage until the applied field is increased to a certain magnitude that seems to be related to the lower critical field H_{c1}.

Similar measurements were done using the same coils and the same sample in a normally conducting state at 13 K in which the EMAT mechanism is effective and in a perpendicular magnetic field. T-coil currents generate eddy currents in the near surface region. These currents experience Lorentz forces in a static magnetic field. It has been found to be a good approximation for normally conducting metals that Lorentz forces can be considered to be directly applied to the solid and thereby generate ultrasonic waves. Ultrasonic waves are detected through the inverse physical process. It is well known[12,14] that in a perpendicular field only shear waves can be generated and detected, and the overall conversion efficiency is proportional to the square of the static magnetic field, $A=KH_{ap}^2$.

Figures 12(a), 12(b), and 12(c) were obtained in the normal state at 13 K under applied magnetic fields H_{ap} of 0.5 kG, 2 kG, and 5 kG, respectively, during the increasing dc-magnetic field stage. $S_{1,5}$ and $S_{2,4}$ are the fifth- and fourth-order shear resonance. No longitudinal waves but only shear waves are obtained, as is evident in Figs. 12(a), 12(b), and 12(c). Figures 13(b) and 13(c), respectively, show the shear-wave amplitudes at resonance for $S_{1,5}$ and $S_{2,4}$ versus the applied dc magnetic field H_{ap} at 13 K. All the data points for

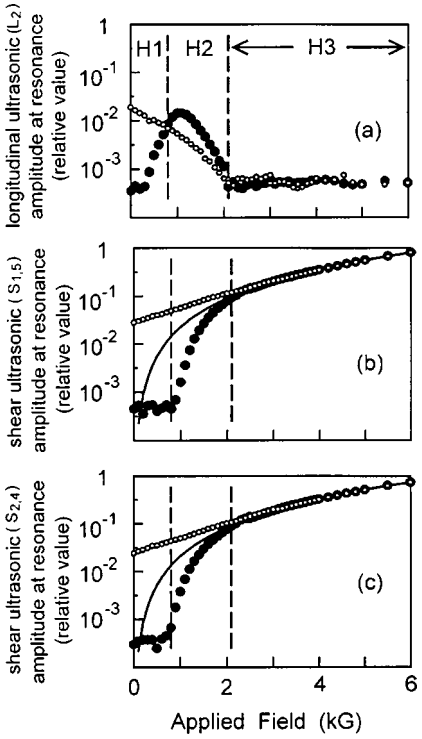

FIG. 9. Resonant peak amplitude of contact-free ultrasonics vs the applied dc magnetic field H_{ap} at 5 K. The sample was cooled in zero field (ZFC) down to 5 K, and then a uniform dc magnetic field was applied perpendicular to the disk plane. (a) The second-order longitudinal resonant peak L_2, (b) the fifth-order shear resonant peak $S_{1,5}$, and (c) the fourth-order shear resonant peak $S_{2,4}$. Solid circles and open circles correspond to increasing and decreasing fields, respectively. The thin solid curve in (b) and (c) is a square law curve $A \propto H_{ap}^2$.

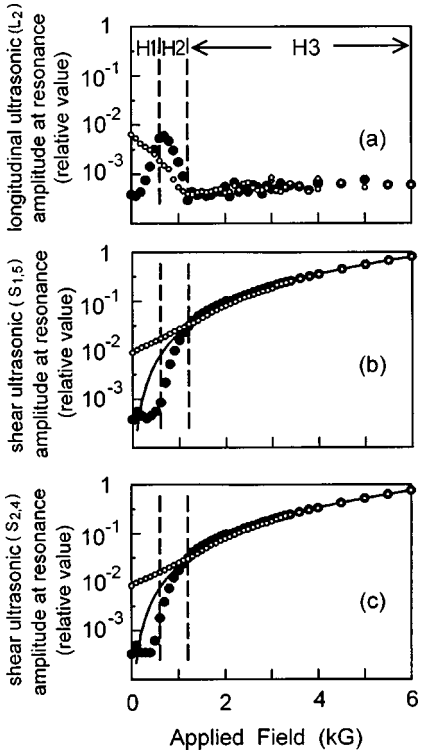

FIG. 10. Resonant peak amplitude for contact-free ultrasonics vs the applied dc magnetic field H_{ap} at 6 K. The sample was cooled in zero field (ZFC) down to 6 K, and then a uniform dc magnetic field was applied perpendicular to the disk plane. (a) The second-order longitudinal resonant peak L_2, (b) the fifth-order shear resonant peak $S_{1,5}$, and (c) the fourth-order shear resonant peak $S_{2,4}$. Solid circles and open circles correspond to increasing and decreasing fields, respectively. The thin solid curve in (b) and (c) is a square law curve $A \propto H_{ap}^2$.

both increasing and decreasing fields fit almost perfectly to the thin solid curve $A = KH_{ap}^2$ and no hysteretic effects are observed as expected. Comparison of Figs. 4, 7, 8 and Fig. 12 and comparison of Figs. 5, 9, 10 and Fig. 13 emphasize how different the polarizations of the ultrasonic waves are for the superconducting state and normal state.

DISCUSSION

Equation (11) can be used in the special case of disk coils and a disk sample provided that the vortex lines are spatially distributed symmetrically with respect to the center axis and the angle α is either 90° or 0°. Here we discuss a different case in which the angle α is neither 90° nor 0°.

The screening current distribution made by a one-loop coil was calculated in Ref. 16. For such a loop coil the screening current distribution is not constant and has a peak just beneath the loop of a coil. In the experiment reported here, the T and R coils are placed at a very small distance from the superconductor disk. The ratio of the coil diameter to the distance is about 32 (the coil diameter is 6.5 mm and the distance is 0.2 mm). The diameter of the coil is much smaller than the superconductor by a factor of about 2 (the sample diameter is 12 mm). In such a case we can assume a moderately constant screening current distribution beneath the coil, with small peripheral effects. Although we assume the penetrated vortex lines are spatially distributed with axial symmetry, one may not assume that the distribution is constant along the radial direction. In another words, the tangential and normal components F_{ST} and F_{SN} of the surface force are spatially distributed with axial symmetry, but these will vary along the radial direction. Consider a small area of the T coil and an area of the same size of the R coil directly opposite one another with respect to the sample. We take the small area dimension to be large compared to the distance (0.2 mm) between the coil and the surface of the supercon-

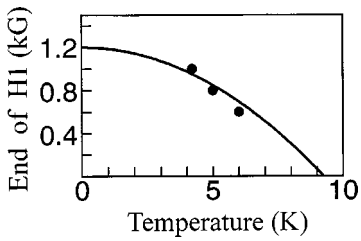

FIG. 11. The end value of the first magnetic field range $H1$ vs temperature. The thin solid curve is drawn using $H_{c1}(T) = H_{c1}(0)\{1-(T/T_c)^2\}$, where $H_{c1}(0)$ and T_c are taken as 1.2 kG and 9.25 K, respectively.

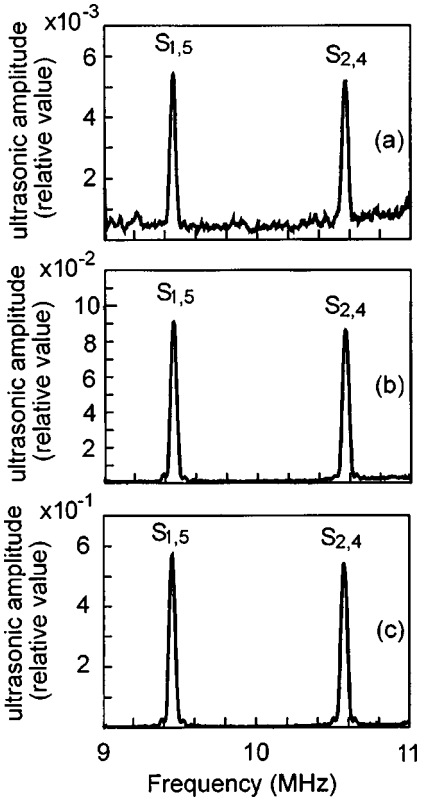

FIG. 12. Resonant peaks for contact-free ultrasonics obtained on single-crystal Nb in the normal state (13 K). $S_{1,5}$ and $S_{2,4}$ are the fifth- and fourth-order shear resonances. Only shear waves were obtained (a) under 0.5 kG, (b) under 2 kG, and (c) under 5 kG.

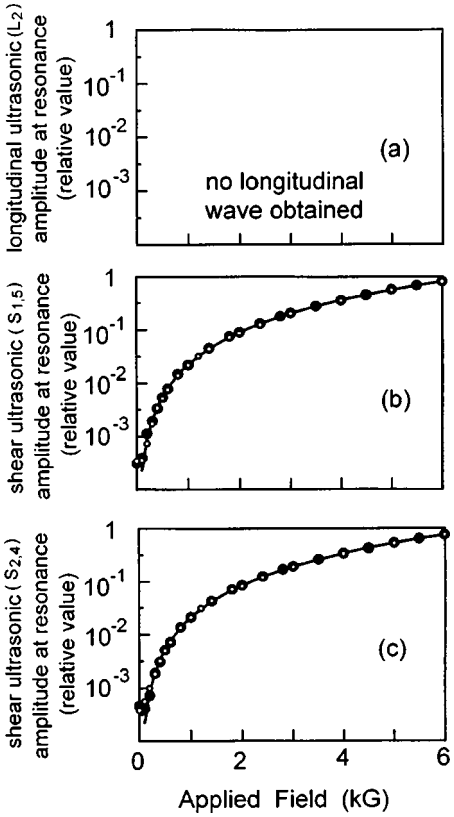

FIG. 13. Resonant peak amplitude for contact-free ultrasonics vs the applied dc magnetic field H_{ap} in the normal state at 13 K. (a) No longitudinal wave obtained, (b) the fifth-order shear resonant peak $S_{1,5}$, and (c) the fourth-order shear resonant peak $S_{2,4}$. Solid circles and open circles correspond to increasing and decreasing fields, respectively. The thin solid curve in (b) and (c) is a square law curve $A \propto H_{ap}^2$.

ductor disk, but small enough to assume a nearly constant surface force distribution in the superconductor surface just beneath it. Such a small area can be assumed to be a part of an infinite plane coil. The tangential and normal components F_{ST} and F_{SN} of the surface force F_S are depicted in Fig. 3(a), and the forces are also shown in Fig. 3(b) together with the small area. F_{SN} generates a longitudinal wave. F_{ST} is divided into two mutually orthogonal in-plane components F_{STX} and F_{STY}, and generates two shear waves through the acoustic birefringence effect. The two shear waves are polarized along the orthogonal directions [001] and $[1\bar{1}0]$, respectively. Here the [001], [110], and $[1\bar{1}0]$ directions coincide with the x, y, and z axes, respectively. Let θ be an angle between the [001] direction and the direction of the small wire element within the small area. In that case

$$F_{STX} = F_{ST} \sin\theta, \tag{12}$$

$$F_{STY} = F_{ST} \cos\theta. \tag{13}$$

Assuming that the penetrated vortex lines are spatially distributed with axial symmetry, the vortex line density can be expressed by $n(r)$ and the angle by $\alpha(r)$, where r is measured from the coil center.

The voltage amplitude e_l detected by the small area dS of the R coil for longitudinal ultrasonic waves is given by using Eq. (9):

$$\begin{aligned} e_l &= K_3 i \exp(-ik_l d) b_0 [n(r)\phi_0 \sin\alpha(r)]^2 dS/\lambda_{ac}\rho V_l \\ &= K_4 [n(r)\sin\alpha(r)]^2 dS, \end{aligned} \tag{14}$$

where $K_4 = K_3 i \exp(-ik_l d) b_0 \phi_0^2/\lambda_{ac}\rho V_l$. Here V_l and k_l are the speed and wave number of the longitudinal ultrasonic wave, respectively.

The voltage amplitude E_l detected by the R coil for longitudinal waves is obtained by integrating Eq. (14) over the coil area:

$$\begin{aligned} E_l &= K_4 \int_S [n(r)\sin\alpha(r)]^2 dS \\ &= K_4 \int_0^{2\pi} \int_0^{r_1} [n(r)\sin\alpha(r)]^2 r\,dr\,d\theta \\ &= K_4 \int_0^{2\pi} d\theta \int_0^{r_1} [n(r)\sin\alpha(r)]^2 r\,dr, \end{aligned} \tag{15}$$

where r_1 is the coil radius. We need to make another assumption that all the penetrated vortex lines have nearly the same angle α to the surface normal within the ac penetration depth range. This assumption is not realistic if used for all angles. But we make this assumption only in a limited case. We

obtained in the experiment no shear waves but only longitudinal waves in a perpendicular magnetic field during the virgin magnetization stage, and this experimental fact strongly suggests that α is nearly 90°. We use this assumption only in this limited situation when α is nearly 90°.

Then Eq. (15) becomes

$$E_l = 2\pi K_4 \sin^2\alpha \int_0^{r_1} [n(r)]^2 r dr. \tag{16}$$

The voltage amplitude $e_{s[001]}$ detected by the small area dS of the R coil for the shear ultrasonic wave polarized along [001] is given by using Eq. (10):

$$\begin{aligned} e_{s[001]} &= K_3 i \exp(-ik_{s[001]}d) b_0 [n(r)\phi_0 \cos\alpha(r)]^2 \\ &\quad \times \sin^2\theta dS/\lambda_{ac}\rho V_{s[001]} \\ &= K_5 [n(r)\cos\alpha(r)]^2 \sin^2\theta\, dS, \end{aligned} \tag{17}$$

where $K_5 = K_3 i \exp(-ik_{s[001]}d) b_0 \phi_0^2/\lambda_{ac}\rho V_{s[001]}$. Here $V_{s[001]}$ and $k_{s[001]}$ are the speed and wave number of the shear ultrasonic wave polarized along the [001] direction, respectively.

The term $\sin^2\theta$ appears in Eq. (17) because both the generating and detecting efficiencies must be multiplied by $\sin\theta$.

The voltage amplitude $E_{s[001]}$ detected by the R coil for the shear ultrasonic wave polarized along [001] is obtained by integrating Eq. (17) over the coil area:

$$\begin{aligned} E_{s[001]} &= K_5 \int_S [n(r)\cos\alpha(r)]^2 \sin^2\theta\, dS \\ &= K_5 \int_0^{2\pi}\int_0^{r_1} [n(r)\cos\alpha(r)]^2 \sin^2\theta\, r dr\, d\theta \\ &= K_5 \int_0^{2\pi} \sin^2\theta\, d\theta \int_0^{r_1} [n(r)\cos\alpha(r)]^2 r dr. \end{aligned} \tag{18}$$

Using the same assumption for $\alpha(r)$, Eq. (18) becomes

$$E_{s[001]} = \pi K_5 \cos^2\alpha \int_0^{r_1} [n(r)]^2 r dr. \tag{19}$$

In a similar manner the voltage amplitude $E_{s[1\bar{1}0]}$ detected by the R coil for the shear ultrasonic wave polarized along $[1\bar{1}0]$ is

$$\begin{aligned} E_{s[1\bar{1}0]} &= K_6 \int_S [n(r)\cos\alpha(r)]^2 \cos^2\theta\, dS \\ &= \pi K_6 \cos^2\alpha \int_0^{r_1} [n(r)]^2 r dr, \end{aligned} \tag{20}$$

where $K_6 = K_3 i \exp(-ik_{s[1\bar{1}0]}d) b_0 \phi_0^2/\lambda_{ac}\rho V_{s[1\bar{1}0]}$. Here $V_{s[1\bar{1}0]}$ and $k_{s[1\bar{1}0]}$ are the speed and wave number of the shear ultrasonic wave polarized along the $[1\bar{1}0]$ direction, respectively.

The absolute values of the ratio of E_l to $E_{s[001]}$ and that of E_l to $E_{s[1\bar{1}0]}$ are calculated from Eqs. (16), (19), and (20) as

$$|E_l/E_{s[001]}| = 2(V_{s[001]}/V_l)\tan^2\alpha, \tag{21}$$

$$|E_l/E_{s[1\bar{1}0]}| = 2(V_{s[1\bar{1}0]}/V_l)\tan^2\alpha. \tag{22}$$

Since the shear ultrasonic-wave signal $E_{s[1\bar{1}0]}$ is not yet detected at the end of $H1$ in Fig. 5(a), we can say that either there exists no shear ultrasonic wave there or $E_{s[1\bar{1}0]}$ is so small that it is hidden under the noise level N.

If $E_{s[1\bar{1}0]}$ exists, but is hidden under the noise level N, α can be roughly estimated. The ratio of the longitudinal wave signal E_l to the noise signal E_n of N at the end of $H1$ is about 33 [Figs. 5(a) and 5(b)], and therefore α is estimated to be at least larger than 82°. This value is obtained as follows:

$$\begin{aligned} \alpha &= \tan^{-1}[\sqrt{(E_l/E_{s[1\bar{1}0]})(V_l/2V_{s[1\bar{1}0]})}] \\ &> \tan^{-1}[\sqrt{(E_l/E_n)(V_l/2V_{s[1\bar{1}0]})}] \\ &= \tan^{-1}[\sqrt{33\times\{5220/(2\times 1930)\}}] \approx 82°. \end{aligned} \tag{23}$$

Since this angle applies to the end of $H1$, it represents a minimum value. The angle will therefore be much closer to 90° at lower fields.

To our knowledge no existing theories have predicted these phenomena and neither have any other known observation techniques revealed them. There have been significant recent developments on the theory of vortex line penetration into a platelet in a perpendicular magnetic field.[1–5,17,18] The critical-state model solution for a circular disk characterized by an arbitrary critical current $j_C(B)$ was given, but only finite values for perpendicular components of flux density were calculated.[1] In the geometrical barrier model a thin superconducting strip of rectangular cross section in a perpendicular field was treated both in the absence and in the presence of pinning, but only finite values for perpendicular field density B_z were calculated.[2,3] An interesting phenomenon predicted for superconductor strips and disks of finite thickness is a ''current string,'' but no such phenomenon as observed in the present paper was treated.[4] An exact analytical solution was given for the critical-state problem in long thin superconductor strips,[5] but only the perpendicular finite component B_z was computed. Very similar vortex line configurations to that inferred here were calculated,[17,18] but the theory was given on the assumption of zero lower critical field H_{c1}, valid only if $|H| \gg H_{c1}$ everywhere inside the superconductor.

Most magnetic measurements on superconductors are carried out by techniques relying on spatial integration, such as magnetometry and ac suceptibility. It is difficult to detect the local vortex line distribution with these methods. There have been significant advances in experimental techniques[19–29] to map vortex line distributions at surfaces, by means of decoration techniques,[19] Hall probes,[20,21] scanning tunneling microscopy,[22] scanning superconducting quantum interference device (SQUID) microscopy,[23] and magnetic-force microscopy.[24] These techniques can only detect the ends of vortex lines at the sample surface but not those lying inside and parallel to the superconductor surface. The magneto-optical technique[25,26] can detect magnetic fields inside a thin sample but cannot detect individual vortices. The Faraday

effect used in this technique detects vortex lines parallel to the direction of the propagation of the normally incident linearly polarized light so that it is very difficuilt to detect vortex lines parallel to the surface. Electron holography and Lorentz microscopy techniques[27–29] detected individual vortex lines inside superconductors and oblique to the sample surface, and also detected Josephson vortices parallel to the surface. The phenomenon described in this paper has not been detected so far by these two techniques.

Similar phenomena were observed by one of the authors in a polycrystalline Nb disk,[30] but the experiment was done only at one temperature (4.2 K), precluding the deduction of general trends as in the present single-crystal case. In conclusion, since the phenomenon observed here affects various experimental results, it should especially not be neglected for the correct interpretation of the results of magnetic measurements in superconductor disk samples.

A similar experiment using high-temperature superconductor samples is the subject of future work. Considering the practical importance of the problem of the magnetization of a thin superconducting platelet in a perpendicular field it is hoped that this system will be investigated in detail, theoretically and experimentally.

[1] D. V. Shantsev, Y. M. Galperin, and T. H. Johansen, Phys. Rev. B **60**, 13 112 (1999).

[2] E. Zeldov, A. I. Larkin, V. B. Geshkenbein, M. Konczykowski, D. Majer, B. Khaykovich, V. M. Vinokur, and H. Shtrikman, Phys. Rev. Lett. **73**, 1428 (1994).

[3] M. Benkraouda and J. R. Clem, Phys. Rev. B **53**, 5716 (1996).

[4] M. V. Indenbom, Th. Schuster, H. Kuhn, H. Kronmüller, T. W. Li, and A. A. Menovsky, Phys. Rev. B **51**, 15 484 (1995).

[5] G. P. Mikitik and E. H. Brandt, Phys. Rev. B **62**, 6812 (2000).

[6] H. Haneda and T. Ishiguro, Appl. Phys. Lett. **68**, 3335 (1996).

[7] H. Haneda, T. Ishiguro, S. Watauchi, J. Shimoyama, and K. Kishio, J. Phys. Soc. Jpn. **67**, 1391 (1998).

[8] E. H. Brandt, Phys. Rev. Lett. **67**, 2219 (1991).

[9] E. H. Brandt, Rep. Prog. Phys. **58**, 1465 (1995).

[10] M. W. Coffey and J. R. Clem, Phys. Rev. B **46**, 11 757 (1992).

[11] N. Lütke-Entrup, B. Plaçais, P. Mathieu, and Y. Simon, Phys. Rev. Lett. **79**, 2538 (1997).

[12] K. Kawashima and O. B. Wright, J. Appl. Phys. **72**, 4830 (1992).

[13] R. F. S. Hearmon, *Numerical Data and Functional Relationships in Science and Technology 11* (Springer-Verlag, Berlin, 1979).

[14] R. B. Thompson, IEEE Trans. Sonics Ultrason. **SU-25**, 340 (1973).

[15] *Handbook of Chemistry and Physics*, 83rd ed., edited by D. R. Lide (CRC Press, Boca Raton, 2002).

[16] J. Gilchrist and E. H. Brandt, Phys. Rev. B **54**, 3530 (1996).

[17] E. H. Brandt, Phys. Rev. B **58**, 6506 (1998).

[18] G. P. Mikitik and E. H. Brandt, Phys. Rev. B **62**, 6800 (2000).

[19] P. L. Gammel, D. J. Bishop, G. J. Dolan, J. R. Kwo, C. A. Murray, L. F. Schneemeyer, and J. V. Waszczak, Phys. Rev. Lett. **59**, 2592 (1987).

[20] Z. Koziol, Z. Tarnawski, and J. Franse, Solid State Commun. **85**, 991 (1993).

[21] W. Xing and B. Heinrich, J. Appl. Phys. **76**, 4244 (1994).

[22] H. F. Hess, C. A. Murray, and J. V. Waszczak, Phys. Rev. Lett. **69**, 2138 (1992).

[23] C. C. Tsuei, J. R. Kirtley, C. C. Chi, L. S. Yu-Jahnes, A. Gupta, T. Shaw, J. Z. Sun, and M. B. Ketchen, Phys. Rev. Lett. **73**, 593 (1994).

[24] A. Moser, H. J. Hug, I. Parashikov, B. Stiefel, O. Fritz, H. Thomas, A. Baratoff, H.-J. Güntherodt, and P. Chaudhari, Phys. Rev. Lett. **74**, 1847 (1995).

[25] Th. Schuster, M. V. Indenbom, H. Kuhn, E. H. Brandt, and M. Konczykowski, Phys. Rev. Lett. **73**, 1424 (1994).

[26] M. R. Koblischk and R. J. Wijngarden, Supercond. Sci. Technol. **8**, 199 (1995).

[27] A. Tonomura, *Electron Holography*, 2nd ed. (Springer, Heidelberg, 1999).

[28] A. Tonomura, H. Kasai, O. Kamimura, T. Matsuda, K. Harada, Y. Nakayama, J. Shimoyama, K. Kishio, T. Hanaguri, K. Kitazawa, M. Sasase, and S. Okayasu, Nature (London) **412**, 620 (2001).

[29] A. Tonomura, H. Kasai, O. Kamimura, T. Matsuda, K. Harada, T. Yoshida, T. Akashi, J. Shimoyama, K. Kishio, T. Hanaguri, K. Kitazawa, T. Masui, S. Tajima, N. Koshizuka, P. L. Gammel, D. Bishop, M. Sasase, and S. Okayasu, Phys. Rev. Lett. **88**, 237001 (2002).

[30] K. Kawashima, Phys. Rev. B **58**, 490 (1998).